Acoustic particle trapping driven by axial primary radiation force in shaped traps

L. Malik,[1] A. Nath,[1] S. Nandy,[1] T. Laurell,[3] and A. K. Sen[1,2,*]

[1]*Fluid Systems Lab, Dept. of Mechanical Engineering, Indian Institute of Technology Madras, Chennai-600036, India*

[2]*Micro Nano Bio –Fluidics Group, Indian Institute of Technology Madras, Chennai-600036, India*

[3]*Division of Nanobiotechnology, Department of Biomedical Engineering, Lund University, Lund University, 221 84 Lund, Sweden*

(Received 10 October 2021; revised 7 January 2022; accepted 17 February 2022; published 8 March 2022)

We study particle trapping driven by the axial primary radiation force (A-PRF) in shaped traps exposed to standing bulk acoustic waves (S-BAW) using numerical simulations and experiments. The utilization of the stronger A-PRF as the main retention force is a consequence of standing-wave formation along the flow direction, instead of the orthogonal direction as in the case of traditionally used lateral-PRF S-BAW trapping setups. The study of particle dynamics reveals that the competition between A-PRF and viscous drag force governs particle trajectory. The ratio of the acoustic energy to the viscous work (β) provides a general criterion for particle trapping at a distinctive off-node site that is spatially controllable. Particles get trapped for $\beta \geqslant \beta_{cr}$ at some distance away from the nodal plane and the distance varies as β^{-c} ($c = 0.6$–1.0). The use of A-PRF as the retention force could potentially allow traditional S-BAW trapping systems to envisage high-throughput advancements surpassing the current standards in cell-handling unit operations.

DOI: 10.1103/PhysRevE.105.035103

I. INTRODUCTION

Ultrasonic standing-wave (USW) technology has emerged as an attractive tool for handling bioparticles in lab-on-a-chip and microfluidic systems in the recent past [1]. Contactless, biocompatible, gentle, and noninvasive manipulation offered by USW in sophisticated cell-based systems outstands itself in the ever-advancing biomedical research [2,3]. Nonlinear effects of scattering of sound waves by small objects present inside acoustofluidic devices [4] generate time-averaged acoustic forces [5] causing acoustophoretic motions [6] that allow size-, density-, and compressibility-based label-free manipulation [7–18] of such objects. Advances [19,20] in cell, particle, and droplet [21–23] handling microfluidic systems pivot around efficient techniques of capturing and immobilizing them [24,25]. Trapping sites serve as flexible chemical microenvironments for microfluidics-based cellular studies such as bioassays [3,26], cell population [27,28], multicell interaction, extraction [2,29], culturing [30], screening and enrichment [2], and washing [2] of cellular entities. Integral to these studies—the need for precise spatial positioning [31,32] and selective manipulation [15] of the trapped objects remains the most sought-after feature among various contact and noncontact-based trapping methods.

The most common contact-based trapping technique is the well-known patch-clamp method [33] suitable for single-object studies wherein the object is captured against an orifice. Both passive and active contactless techniques have been widely utilized for handling single-particle and cluster traps [34]. Contactless trapping of bioparticles facilitates delicate cell-based studies [28] in flexible stress-free culture environments, wherein minimal cellular perturbations enable studying nonadherent cells in an *in vivo* setting [32]. Contactless retention methods fundamentally involve immobilizing particles by an imposed force field versus the fluidic viscous force. The field may however originate externally from dielectrophoretic [35], magnetic [36], optical [37], acoustic [10,38] effects, or the innate hydrodynamics [39] of the flow system.

Optical traps retain particles through a precisely focused laser beam whose motion controls the desired translation of the trapped objects [37]. Dielectrophoresis (DEP) traps [40] are governed by the dielectric forces experienced by particles exposed to a nonuniform electrical field. Magnetic traps [41] utilize the presence of a nonuniform magnetic field to trap magnetic particles. On the other hand, in acoustic trapping, particles experience acoustic radiation force in microfluidic chambers geometrically designed to sustain standing waves (SW) upon ultrasonic actuation. Acoustic trapping offers a contactless technique to immobilize, position, and retain particles at defined locations. Compared to other contactless trapping techniques, acoustic trapping setup relishes several advantages: it is most suitable for miniaturization and therefore gets smoothly facilitated in microfluidic systems unlike optical tweezers; does not involve complicated, bulky, or expensive setup; allows handling of a large number of cells at a higher operating flow rate, offering high-throughput unlike optical tweezers and DEP traps; allows for long retaining times with preserved cell viability unlike optical laser traps which may pose thermal damage [42]; works with most particles unlike magnetic and DEP traps which require specific particle properties or buffer conditions [35]. Furthermore, unlike other trapping techniques, it is independent of the type of media, the only requisite being a difference in density and/or compressibility of the particle that gives rise to a nonzero acoustic contrast factor in the chosen media, which is the common case in most particle (cell) handling operations. Owing to these benefits, there have been several attempts to

*ashis@iitm.ac.in

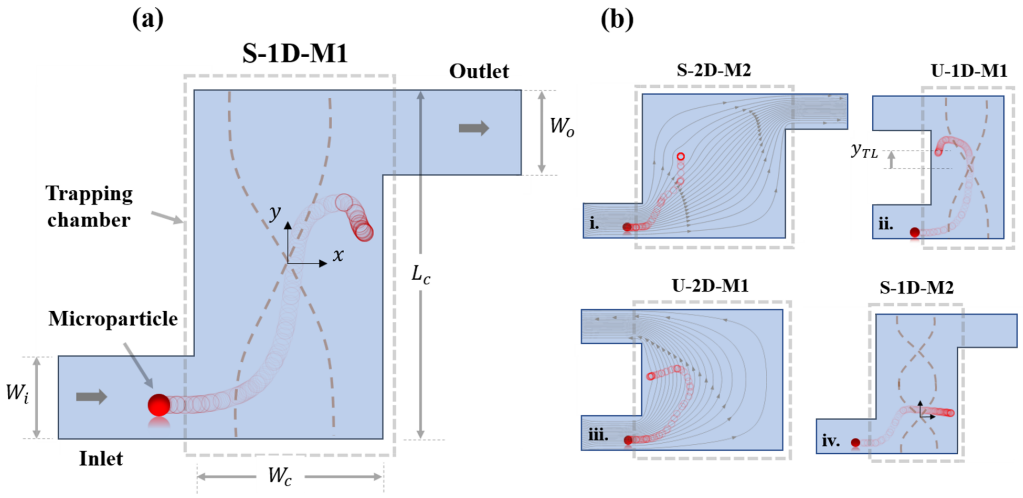

FIG. 1. (a) Schematic of an S-shaped trap comprising an inlet channel, a trapping chamber, and an outlet channel, exposed to 1D SW operating at the first harmonic mode (M1), i.e., half-wave mode, S-1D-M1 with the pressure nodal plane at $y = 0$. The width of the inlet and outlet channels are W_i and W_o, respectively. The length and width of the trapping chamber are L_c and W_c, respectively. (b) Schematic of the various shaped traps: i. S-shaped trap with 2D SW in second harmonic mode (M2), S-2D-M2; ii. U-shaped trap with 1D SW in first harmonic mode, U-1D-M1; iii. U-shaped trap with 2D SW in first harmonic mode, U-2D-M1, and iv. S-shaped trap with 1D SW in second harmonic mode, S-1D-M2. The other configurations: S-2D-M1, S-2D-M3, S-1D-M3, U-1D-M2, U-1D-M3, U-2D-M2, and U-2D-M3, are also used in the present study but are not shown here for brevity. Representative trajectories (red circles) and trapping locations of particles in various configurations are also shown in the schematic. Sinusoidal dashed curves shown in (a) and (b)-ii, (b)-iv represent the standing-wave formation. Streamlines at the final trapped instant, shown in (b)-i, (b)-iii, reveal fluid flow in the chambers. The density of streamlines shown is controlled via velocity magnitude and arrows pointing in the flow direction are kept of uniform size for illustration purposes.

develop acoustic particle trapping [43] techniques predominantly for the study of particle aggregates [44], particle-based bioassays [26], cell population studies [27,28], enrichment of dilute samples [2], and seed particle enabled nanoparticle capture [45].

Particle trapping in the traditional standing bulk acoustic waves (S-BAW) setup having the standing wave aligned perpendicular to the flow direction [3,4,8,23,45–47] utilizes first, the axial component of the primary radiation force (A-PRF) acting along the wave direction to bring the particles closer to the pressure node, and further, the lateral PRF (L-PRF) which is a few orders of magnitude smaller than the A-PRF, is used as the main retention force for trapping the particles against the flow [48]. To achieve efficient lateral trapping, it is necessary to have a high lateral gradient of acoustic energy density, which is mostly facilitated either with a miniaturized transducer-based highly localized acoustic field [3,8,49] or with a resonance cavity-based localized resonance [32,50,51]. Despite such efforts and weaker retention force, traditional S-BAW trapping devices adopt the L-PRF ($\sim$100 pN) as the main trapping force. Although more recent and advanced trapping systems such as acoustical beam traps [13] offer high lateral trapping force, lateral force in the traditional S-BAW systems is weaker as compared to the A-PRF. Particle trapping in the traditional S-BAW systems using A-PRF ($\sim$10 nN) capable of allowing operation over a wider range of flow rates is not yet explored in literature. Further, most of the current S-BAW systems lack flexibility in terms of precise control and/or choice of trapping locations, although complex trapping designs with a drive-frequency modulation [50], phase-controllable transducers [52], or subset transducers arrays [46] offer variable trapping positions. A simple trapping arrangement utilizing the relatively stronger A-PRF [53,54] for particle trapping in a traditional S-BAW setup with a deterministic spatial control over the trapping location has not received attention to date. Also, a theoretical [55] understanding of the trapping phenomenon, involving analysis of the forces and energies involved, as well as a general criterion for particle trapping using A-PRF, is not available.

Here, we study the dynamics of particle trapping driven by A-PRF in shaped traps using numerical simulations and experiments. Particle trapping using A-PRF in place of the commonly used L-PRF is attributed to the standing-wave formation along the flow direction. We characterize the trapping phenomenon in terms of particle trajectory and velocity variations with time and show that trapping is the consequence of a balance between A-PRF and fluidic viscous force. Irrespective of the operating conditions, the trapping phenomenon is generalized in terms of acoustic energy to viscous work ratio, β. We study the particle trajectory and trapping location by considering the effect of the initial particle streamline position, the geometry of the shaped trap, standing-wave pattern, harmonic modes, and the parameter, β.

II. THEORETICAL

The shaped trap used in the present study comprises an inlet channel, a trapping chamber exposed to S-BAW, and an outlet channel. The schematic of an S-shaped trap exposed to one-dimensional (1D) S-BAW is shown in Fig. 1(a). The chamber is placed sufficiently away from the inlet and outlet regions to eliminate any effect of flow perturbations close to the inlet (outlet) on particle trapping. Various designs of shaped traps with different inlet (outlet) configurations such

as S- and U types, standing-wave patterns, i.e., 1D or two-dimensional (2D), and harmonic modes such as half wave (indicated as M1) and full wave (indicated as M2), are presented in Fig. 1(b). A particle flowing through the trapping chamber experiences A-PRF in addition to the fluidic viscous force and a balance between the two forces leads to particle trapping. Depending upon the design of the shaped trap, different particle trajectories and trapping locations are observed. Typical particle trajectories and trapping locations in different shaped traps are shown in Fig. 1. Here, we outline a general theory describing the particle-trapping phenomenon in a 2D field.

Acoustic migration of particles inside a channel mainly relies on the primary radiation force (PRF) that emerges due to the scattering effects when particles are exposed to the standing-wave field. In 1962, Gor'kov [56] presented studies on acoustic radiation forces acting on a particle suspended in an inviscid fluid and generalized it for the case of an arbitrary standing-wave field for particle size smaller than the wavelength. Gor'kov acoustic potential (U) for a single particle with acoustic properties different from those of the suspending fluid is used to find the primary radiation force ($\mathbf{F}_A$) as follows:

$$\begin{aligned}\mathbf{F}_A &= -\nabla U \\ &= -V_p \nabla\left[f_1\langle \mathrm{PE}\rangle - \frac{3f_2}{2}\langle \mathrm{KE}\rangle\right] \\ &= -\frac{V_p}{4\rho_f c_f^2}\nabla\left[2f_1\langle p_1^2\rangle - \frac{3f_2}{k^2}\langle|\nabla p_1|^2\rangle\right],\end{aligned} \tag{1}$$

where V_p is the volume of the spherical particle of radius $a(=D/2)$, f_1 and f_2 are constant factors given by Eq. (2), $\langle \mathrm{PE}\rangle = 0.5\,\beta_f\langle p_1^2\rangle$ and $\langle \mathrm{KE}\rangle = 0.5\,\rho_f\langle|\mathbf{v}_1^2|\rangle$ are the time-averaged potential and kinetic energy densities, respectively, with $\mathbf{v}_1$ being the acoustic velocity field, k is the wave number given by Eq. (3) with k_x and k_y referring to the wave numbers in corresponding directions given by Eq. (4), p_1 is the acoustic pressure field, which for a two-dimensional plane wave [57] with a uniform pressure amplitude p_a with origin at the center of the two-dimensional cavity is given by Eq. (5), ρ is density, $\beta = 1/\rho c^2$ is compressibility, c is sound velocity, and subscripts p and f denote the particle and fluid medium, respectively. Symbol $\langle\ \rangle$ in Eq. (1) and all subsequent equations refers to the corresponding time-averaged quantities.

$$f_1 = 1 - \frac{\beta_p}{\beta_f}, \quad f_2 = \frac{2(\rho_p - \rho_f)}{\rho_f + 2\rho_p}, \tag{2}$$

$$k^2 = k_x^2 + k_y^2, \tag{3}$$

$$k_x = n\frac{\pi}{W_c}, \quad k_y = m\frac{\pi}{L_c} \tag{4}$$

$$\begin{aligned}p_1(x,y) &= p_a \cos\theta_x \cos\theta_y \\ &= p_a \cos\left(k_x x + \frac{n\pi}{2}\right)\cos\left(k_y y + \frac{m\pi}{2}\right).\end{aligned} \tag{5}$$

Factors n and m in Eqs. (4) and (5) are nonzero integers indicating the harmonic mode, where $n = 2, 3\ldots$ and $m = 2, 3\ldots$ indicate higher-resonance modes along x and y, respectively. Also, W_c and L_c in Eqs. (4) refer to the width and length of the trapping chamber in x and y directions (refer to Fig. 1). In the first harmonic mode (M1), the pressure nodal plane [Figs. 1(a) and 1(b)-ii] or region [Fig. 1(b)-iii] lies at the center of the chamber.

For a one-dimensional plane standing wave generated along the y direction as in the case of a one-dimensional chamber [refer to Figs. 1(a) and 1(b)-ii], Eqs. (3) and (5) reduce to $k = k_y$ and $p_1(y) = p_a \cos\theta_y$, respectively. Further, by evaluating Eq. (1), the expression for A-PRF acting along the y direction can be derived as done in literature [5,48], and is given as follows:

$$\langle F_A(y)\rangle = 3\,V_p\,E_{ac}\,k\,\sin(2\theta_y)\,\phi, \tag{6}$$

where $E_{ac} = p_a^2/(4\rho_f c_f^2)$, is the acoustic energy density which is the sum of time-averaged kinetic and potential energy densities, y is the distance from the nearest pressure node, and ϕ is the acoustic contrast factor, given by

$$\phi = \tfrac{1}{3}f_1 + \tfrac{1}{2}f_2. \tag{7}$$

The A-PRF drives the particles with $\phi > 0$ to the pressure nodes and $\phi < 0$ to the pressure antinodes.

Prediction of resonance modes in two-dimensional cavities is not trivial [54]. In two-dimensional geometries [refer to Figs. 1(b)-i and 1(b)-iii] supporting plane standing waves in both x and y directions, Eq. (6) is not valid and hence utilizing Eqs. (1)–(5), we derive (refer to Sec. S1 of the Supplemental Material [58]) general expressions of x and y components of the primary radiation force as given in Eqs. (8) and (9).

$$\begin{aligned}\langle F_A(x)\rangle = 3\,V_p\,E_{ac}\,k_x\,\sin(2\theta_x)\Bigg[&\frac{1}{3}f_1(\cos\theta_y)^2 \\ &+ \frac{1}{2}f_2\left\{(\cos\theta_y)^2 - \left(\frac{k_y}{k}\right)^2\right\}\Bigg],\end{aligned} \tag{8}$$

$$\begin{aligned}\langle F_A(y)\rangle = 3\,V_p\,E_{ac}\,k_y\,\sin(2\theta_y)\Bigg[&\frac{1}{3}f_1(\cos\theta_x)^2 \\ &+ \frac{1}{2}f_2\left\{(\cos\theta_x)^2 - \left(\frac{k_x}{k}\right)^2\right\}\Bigg].\end{aligned} \tag{9}$$

By substituting n (for resonance in the y direction) or m (for resonance in the x direction) equal to zero in Eqs. (8) and (9), these expressions readily reduce to the expression for the one-dimensional case as given in Eq. (6).

In most applications, the objects to be manipulated such as microparticles or cells experience a larger share of force from the potential energy (PE) term in Eq. (1) as compared to the kinetic energy (KE) term [46]. Hence, pressure fields are of more importance to describe the behavior of particles inside acoustically vibrating devices. Due to the positive sign of the PE term, the less compressible particles (than fluid) get driven towards the region of potential energy density minima, the pressure nodal plane. This is attributed to the axial primary radiation force explained earlier in this section. At the pressure nodal plane, the PE term does not contribute to the radiation force because of the presence of zero pressure gradient at the nodal plane and hence the particles do not experience A-PRF. However, the particles at the pressure nodal plane keep experiencing the PRF, howsoever smaller, due to the KE term. The negative sign in the KE term makes

denser (than fluid) particles move towards the region of kinetic energy density maxima, which at the pressure nodal plane is equal to the total acoustic energy density (E_{ac}) maxima. This force originating from the lateral gradients in the velocity field is known as the lateral primary radiation force. In literature, a general expression for L-PRF for a one-dimensional general wave field has been derived from first principles by considering a nonuniform pressure amplitude in the lateral directions [48,59], which is given by

$$\mathbf{F}_L = -V_p \nabla E_{ac} \left[f_1 \sin^2(ky) - \tfrac{3}{2} f_2 \cos^2(ky) \right]. \quad (10)$$

In general, these amplitude variations in the lateral directions could be a consequence of nonuniform source amplitude, wave divergence, and boundary effects. In conventional trapping systems using L-PRF, the lateral gradients (∇E_{ac}) at the pressure nodal planes are mostly present locally in the vicinity of the transducer area and diminish rapidly outside of it. These gradients are highly desired, and hence suitably enhanced through design modifications to enable lateral trapping of particles against the viscous drag. In the traditional S-BAW systems, although $F_L \ll F_A$ elsewhere, but at the nodal plane, $F_A = 0$ and therefore once a particle arrives at the nodal plane, F_L enables particle trapping if it can overcome the fluidic viscous drag force. As discussed in the Introduction, particle trapping using F_L suffers from several limitations and therefore in the present work we make use of F_A to achieve particle trapping by employing a unique shaped-trap arrangement. As shown in Eqs. (6) and (10), unlike F_L, F_A scales with E_{ac} and not its gradient, ∇E_{ac}, and therefore it is at least two orders of magnitude higher than F_L. In the current work, the standing-wave axis and hence F_A are aligned with the flow direction inside the trapping chamber facilitating the trapping of particles against the fluidic viscous force.

Further, in a particle suspension, besides primary acoustic radiation forces, acoustic interaction between neighboring particles through scattered waves can lead to secondary or interparticle radiation forces. The secondary radiation force is typically a few orders of magnitude smaller than the A-PRF, $F_S \ll F_A$. However, at the nodal plane, both the L-PRF, F_L and secondary radiation force, F_S become significant and together govern the positioning of the particle [60]. In the present study, we focus on studying the physics of trapping a single particle where F_S is not relevant. Further, the viscous attenuation of sound waves in a fluid result in a gradient in the time-averaged momentum flux which gives rise to acoustic streaming flows [61]. The acoustic streaming-induced drag scales linearly with the particle size, whereas axial PRF scales with the cube of the particle size which gives a critical particle size below which streaming effect is significant [62]. In the present work, we consider particles of sizes well above the critical value so the streaming effects are negligible. The scaling of the secondary force, and streaming-induced force is presented in the Supplemental Material (Sec. S2). Also, a comparison between streaming and bulk velocity vector fields is presented in the Supplemental Material (Sec. S3).

Neglecting the finite-size effects from the chamber walls, the fluidic drag force acting on a microparticle of diameter D trapped at a position r is approximated by the Stokes relation, $\mathbf{F}_D = 3\pi\eta D\boldsymbol{u}(r)$, which will be balanced by the acoustic force acting on the particle given by Eq. (1), where $\mathbf{u}(r)$ is the fluid velocity at the trapping location, and η is the dynamic viscosity of the fluid medium. So, at the trapping location, the net force $\mathbf{F}_{\text{net}} = \mathbf{F}_D + \mathbf{F}_A$ will be zero and as a result particle velocity $\mathbf{u}_p = 0$. In the present work, although we first consider competition between the axial PRF and the hydrodynamic force to explain the particle dynamics and trapping, their highly dynamic nature makes it difficult to characterize the system based on forces. Therefore, we resort to the competition between the scaled dimensionless acoustic energy and fluidic viscous work involved in the trapping process to analyze the trapping phenomenon. Taking the diameter of the particle as the characteristic distance, the scale of acoustic energy of the particle can be estimated as

$$E_A \equiv E_{ac} k\phi D^3 \cdot D = E_{ac} k\phi D^4 \quad (11)$$

and the fluidic viscous work is scaled as

$$W_V \equiv \eta U D \cdot D = \eta U D^2. \quad (12)$$

E_A and W_V have been nondimensionalized with the initial kinetic energy (KE_i) of the particle before entering the trapping chamber, $\text{KE}_i = 0.5 m v_i^2$ where m is the mass of the particle and v_i is the magnitude of the velocity of the particle before entering the chamber. KE_i is chosen as a scale for nondimensionalizing E_A and W_V, since it is the total energy that the particle possesses before entering the chamber, inside which it gets subjected to the externally applied acoustic energy. The nondimensionalized acoustic energy and viscous work scales are given as E_A^* and W_V^*:

$$E_A^* = \frac{E_A}{\text{KE}_i}, \quad (13)$$

$$W_V^* = \frac{W_V}{\text{KE}_i}. \quad (14)$$

The ratio of the acoustic energy to the viscous work is represented by the dimensionless parameter β as follows:

$$\beta = \frac{E_A}{W_V} = \frac{E_A^*}{W_V^*} = \frac{E_{ac} k\phi D^2}{\eta U}, \quad (15)$$

where U is the average fluid velocity in the trapping chamber. The value of the parameter β is varied extensively by varying all variables (refer to Table S1 in Supplemental Material, Sec. S4) in the expression while keeping ϕ and η fixed, taking polystyrene as the solid medium and 9% iodixanol solution in deionized (DI) water as the suspending fluid medium, respectively [63]. The foregoing characterization of the trapping phenomenon via β is considered for the case of one-dimensional and two-dimensional chambers across trap shapes, S and U for harmonic modes, M1 and M2. For scaling acoustic energy in two-dimensional chambers using Eq. (11), the factor inside the square brackets of Eqs. (8) and (9) is taken to be of the same scale as of ϕ.

III. NUMERICAL MODEL

Two-dimensional simulations are performed to study particle dynamics, predict the trapping and nontrapping regimes,

and determine the trapping location. The particle is assumed to be small enough to have a negligible influence on the acoustic field. The acoustic pressure field inside the chambers is assumed to be of the form given by Eq. (5) and the force fields generated using derived expressions given by Eqs. (8) and (9) are assumed to be valid, and hence employed directly in the finite-element solver. Thus, only the flow dynamics around the solid particle and the resulting drag force field are computed through simulations. The governing equations of the physical model are formulated employing a fully coupled Fluid Structure Interaction (FSI) equipped finite-element based transient solver in COMSOL MULTIPHYSICS 5.5. To simulate the motion of a particle inside a microfluidic trapping chamber, assuming fluid flow to be incompressible and solid particles to have isotropic linear elasticity, the following set of governing equations are used. The continuity equation is given as [64]

$$\rho\ \nabla \cdot \mathbf{u} = 0, \tag{16}$$

where ρ is the fluid's density and $\mathbf{u}$ is the velocity vector field. The momentum equation described by the incompressible Navier-Stokes equation is as follows [64,65]:

$$\rho\frac{\partial \mathbf{u}}{\partial t} + \rho(\mathbf{u}\cdot\ \nabla)\mathbf{u} = \ \nabla \cdot [-p\mathbf{I} + \mu(\nabla\mathbf{u} + (\nabla\mathbf{u})^{\mathbf{T}})] + \mathbf{F} + \mathbf{B} \tag{17}$$

where p is the pressure, μ is the dynamic viscosity of the fluid, $\mathbf{B}$ is the body forces such as gravitational force per unit volume which is neglected in the present study, and $\mathbf{F}$ is an extra drag term in the momentum equation which takes care of the shallow-channel approximation relevant for the two-dimensional formulation, which is given as [39]

$$\mathbf{F} = -\frac{12\mu\mathbf{u}}{H^2}, \tag{18}$$

where H is the channel height. Adding $\mathbf{F}$ in Eq. (8) enables rather improved modeling of shallow rectangular channels as it allows the use of a 2D model over the computationally more expensive three-dimensional model. In this way, the effect of viscous resistance offered by the channel side walls which is normally neglected in a regular 2D simulation is also considered.

The mechanics of the solid particle, namely the strain displacement equation, Newton's equation, and the constitutive law, are described by Eqs. (19)–(21), respectively, as follows [39]:

$$\boldsymbol{\varepsilon}_{\mathrm{s}} = \frac{1}{2}[(\nabla\mathbf{u}_{\mathrm{s}}) + (\nabla\mathbf{u}_{\mathrm{s}})^T + (\nabla\mathbf{u}_{\mathrm{s}})(\nabla\mathbf{u}_{\mathrm{s}})^T], \tag{19}$$

$$\nabla\cdot\boldsymbol{\sigma}_s + \ \mathbf{F}_s + \mathbf{B}_s = \rho_s\frac{\partial^2\mathbf{u}_{\mathrm{s}}}{\partial t^2}, \tag{20}$$

$$\boldsymbol{\sigma}_{\mathrm{s}} = C\boldsymbol{\varepsilon}_{\mathrm{s}}, \tag{21}$$

where $\boldsymbol{\varepsilon}_{\mathrm{s}}$ denotes the infinitesimal strain tensor, $\mathbf{u}_{\mathrm{s}}$ is the displacement field for the solid particle, $\boldsymbol{\sigma}_{\mathrm{s}}$ being the Cauchy stress tensor, $\mathbf{F}_{\mathrm{s}}$ is the body force per unit volume due to fluid load, $\mathbf{B}_{\mathrm{s}}$ is the external body load per unit volume which is specified as the acoustic axial PRF given by Eqs. (6), (8), and (9) as relevant for the one-dimensional and the two-dimensional chambers, and C denotes the stiffness matrix given as,

$$C = \frac{\mathrm{E_s}}{(1+\nu)(1-2\nu)}\begin{bmatrix} 1-\nu & \nu & \nu & 0 & 0 & 0 \\ \nu & 1-\nu & \nu & 0 & 0 & 0 \\ \nu & \nu & 1-\nu & 0 & 0 & 0 \\ 0 & 0 & 0 & 1-2\nu & 0 & 0 \\ 0 & 0 & 0 & 0 & 1-2\nu & 0 \\ 0 & 0 & 0 & 0 & 0 & 1-2\nu \end{bmatrix}, \tag{22}$$

where E_s and ν are elastic modulus and Poisson's ratio of the particle's material, respectively. The FSI model couples the flow dynamics with the solid mechanics capturing the interactions at the boundaries between the fluid and the solid phases. The interface between the fluid domain that uses an Eulerian formulation and a spatial frame with deformed mesh and the solid domain that uses a Lagrangian formulation and a material frame with undeformed mesh is coupled by employing the arbitrary Lagrangian-Eulerian (ALE) method [66]. The FSI model defines the two-way coupled effect of fluid load on the solid and displacement of the solid on the flow field, represented by Eqs. (23) and (24), as follows:

$$\mathbf{f} = -\mathbf{f}_{\mathrm{s}} = \mathbf{n}\cdot\ [-\mathrm{p}\mathbf{I} + \mu(\nabla\mathbf{u} + (\nabla\mathbf{u})^T)], \tag{23}$$

$$\mathbf{u}_{\mathrm{s}}^{'} = \frac{\partial\mathbf{u}_{\mathrm{s}}}{\partial \mathrm{t}} = \mathbf{u} \tag{24}$$

where $\mathbf{f}_{\mathrm{s}}$ is the total force exerted on the solid boundary which is cumulative of the pressure and the viscous force, $\mathbf{f}$ is the reaction force on fluid, $\mathbf{n}$ is the outward normal unit vector to the boundary, and $\mathbf{u}_{\mathrm{s}}^{'}$ is the rate of change of displacement of the solid which equals the fluid velocity $\mathbf{u}$ on the solid-fluid interface, making it behave like a moving no-slip wall for the fluid. Since fluid and solid mechanics equations are defined and solved in different frames, therefore the following force transformation is imperative:

$$\mathbf{F}_{\mathrm{s}} = \mathbf{f}_{\mathrm{s}}\frac{dv}{dV}, \tag{25}$$

where dv and dV are the scale factors of mesh elements in the spatial and material frames, respectively. Equations (15)–(23) are simultaneously solved for unknowns $\mathbf{u}$, p, $\mathbf{u}_{\mathrm{s}}$, $\boldsymbol{\sigma}_{\mathrm{s}}$, and $\boldsymbol{\varepsilon}_{\mathrm{s}}$.

In the present study, an average normal velocity and zero-gauge pressure conditions are prescribed at the inlet and outlet, respectively. No-slip boundary conditions are specified on the solid boundaries including the channel walls and the particle surface. Fluid velocity field, pressure field, solid displacement field, and solid velocity field are all initialized

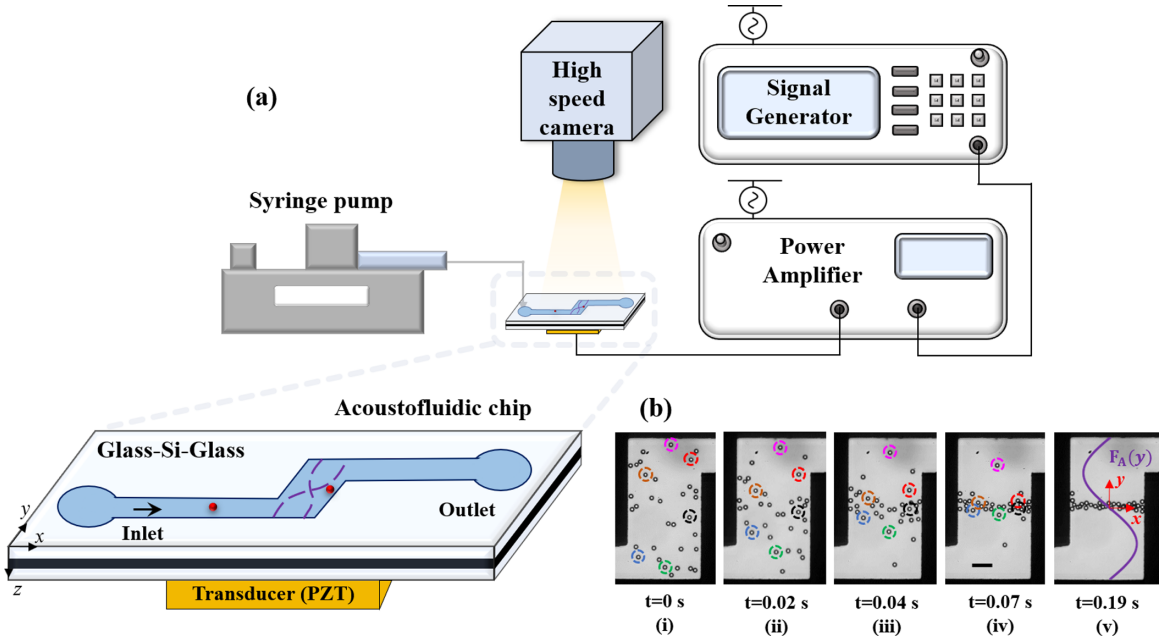

FIG. 2. (a) Schematic of the experimental setup showing the acoustofluidic chip comprising an S-1D-M1 trap with piezoelectric transducer, signal generator and amplifier, syringe pump, and the high-speed camera. (b)-i to (b)-v are successive experimental pictures of 25-μm polystyrene microparticles actuated at 75 J/m^3 migrating towards the central plane of the chamber at the no-flow condition in 9% iodixanol solution in DI water, proving the existence of a nodal plane at $y = 0$ at a resonant frequency of 0.947 MHz. Few particles are encircled with different colors for presentation purpose. Also shown in (b)-v is the sinusoidal variation of the axial primary radiation force F_A along the y direction given by Eq. (6), always pointing towards the nodal plane ($y = 0$) for positive contrast particles. Scale bar represents 100 μm.

with a value equal to zero. Properties of 9% iodixanol in DI water and polystyrene are assigned to the fluid and solid domains, respectively [63]. The properties of the fluid, solid medium, and the range of relevant parameters used in our simulation study are presented in in Table S1 in the Supplemental Material (Sec. S4).

For a given shaped-trap configuration, the computational domain is chosen as per the corresponding schematic shown in Fig. 1. The width of the inlet and outlet channels are $W_i = W_o = 175$ μm and the length and width of the trapping chamber are $L_c = 750$ μm, $W_c = 400$ μm in 1D traps, and $L_c = W_c = 750$ μm in 2D traps, as presented in Table S1 in Supplemental Material (Sec. S4). The motion of a microparticle traversing through the trapping chamber and its interaction with the fluid requires the fluid domain mesh to freely move and deform continuously, as shown in Fig. S2(a) in the Supplemental Material (Sec. S5). For this purpose, a built-in mesh smoothing function [39] is employed to handle the corresponding stretching in the mesh elements of the deforming fluid domain. Moreover, the ALE method combined with the automatic remeshing module ensures the desired mesh quality by recreating the mesh whenever it drops below the set quality criterion, and further the simulation proceeds with the newly generated mesh. A lower value of the set quality criterion can lead to a larger number of inverted elements over a substantial period of the total solution time, thus leading to an overall reduced solution accuracy or even major convergence issues. Therefore, a minimum mesh quality of 0.5 is considered in the present study for obtaining an optimally accurate solution [39]. Based on the grid independence study as shown in Fig. S2(b) in the Supplemental Material (Sec. S5), an appropriate mesh with 17 054 triangular elements, 566 edge elements, 17 vertex elements, average element quality of 0.92, and minimum element quality of 0.58 is chosen for the study. The percentage error in the mesh convergence study is calculated using an extra-fine mesh (having 58 670 triangular elements) chosen for reference. The numerical simulations are analyzed using the built-in postprocessing module in COMSOL MULTIPHYSICS. The location and velocity of the particle are traced by tracking the centroid of the particle.

IV. EXPERIMENT

A schematic of the experimental setup is shown in Fig. 2(a). The device is fabricated in silicon—-the microchannels are etched through the entire thickness of a 200-μm-thick silicon wafer using deep reactive ion etching and sealed by anodically bonding 500-μm glass lids on both sides. The width of the inlet and outlet channels are 175 μm, the length and width of the trapping chamber are 750 and 400 μm, respectively, and the depth is 200 μm throughout. The trapping chamber is located exactly at the center of the channel, measuring 2.25 cm both from the inlet and outlet ports. The inlet and outlet channels are provided with drilled holes through the top glass lid using computer numerical control (CNC) micromilling to enable fluidic access. The particle suspension is prepared by suspending 10 μl of concentrated aqueous solution (having 10% w/v solid particle fraction) of polystyrene microparticles (Sigma-Aldrich, Bangalore, India) into 3 ml of 9% iodixanol (OptiPrep, Sigma-Aldrich, Bangalore, India) solution in DI water, ensuring the beads remain neutrally

buoyant. A very dilute suspension is used to avoid the possibility of clustering of particles due to the trapping of multiple particles, thus facilitating the study of trapping of a single particle. Unless otherwise specified, particles of diameter 25 μm are used in our studies. Particles of diameters 15, 20, 25, and 36 μm are used in the studies presented in Sec. V B. The suspension is introduced into the microfluidic device using a high-performance syringe pump (neMESYS pump, Cetoni, Germany) and a polymer tubing system connecting the pump and the inlet port.

To produce acoustic standing waves, a 2.5 × 2.5 × 0.2-cm plate-type piezoelectric transducer (Sparkler Ceramics, India) with a rated frequency of 1 MHz is bonded to the glass substrate using epoxy resin and a hardener (Loctite Tough X Adhesive, Asian Paints, India) such that its position is symmetric with respect to the location of the trapping chamber as shown in Fig. 2(a). An rf signal generated by a function generator (SMC100A, Rohde & Schwarz, Germany) and amplified by a power amplifier (75A250A, Amplifier Research, USA) is supplied into the system through the transducer. An inverted fluorescent microscope (IX71, Olympus Corporation, Japan) combined with a high-speed camera (SA5, Photron, United Kingdom) is used for visualizing flow and particle trapping.

To find the resonant frequency of the system, the particle suspension is introduced into the microfluidic device and at a stop-flow condition; the actuation frequency is varied over a range of 0.9–1.05 MHz. Upon actuation, the beads rapidly migrate and focus at the pressure nodal plane located at the center of the trapping chamber ($y = 0$) at the resonant frequency in half-wave mode, which is found to be 0.947 MHz [Figs. 2(b)-i to 2(b)-v]. Acoustic energy density is estimated by equating the drag force with the A-PRF acting on microparticles inside the trapping chamber using a previously reported technique [67], for which the particle suspension is infused into the system, and at a stop-flow condition, the particles are exposed to the S-BAW by operating at the resonant frequency. Migration of particles [Figs. 2(b)-i to 2(b)-v] inside the trapping chamber to the pressure node is recorded by the high-speed camera operating at 1000 fps. In the absence of fluid motion, as the particle migration is solely based on the acoustic A-PRF, by tracking the positions of the particles with time, $y(t)$, and analyzing the video using Tracker (Open-Source Physics), the migration velocity (v) is determined. By balancing the A-PRF, $\mathrm{F_A(y)}$ as given by Eq. (6) with the viscous Stokes drag force, $F_D(y) = -6\pi\mu a v$, and adjusting the terms, in case of a one-dimensional chamber [Figs. 1(a) and 2(b)], we get [67]

$$y(t) = \frac{1}{k}\tan^{-1}\left[\tan[ky(0)]\exp\left[\frac{4\phi}{3\mu}(ka)^2 E_{ac} t\right]\right], \qquad (26)$$

where $y(0)$ is the particle position at $t = 0$ s, and $y(t)$ is the particle position at time t. For a given particle's trajectory, we fit the above equation by taking E_{ac} as a fitting parameter to find the best fit of the trajectory of the particle to match the experimental data. We repeat the above method for various other particles to obtain an average value of acoustic energy density at a particular actuation voltage. The acoustic energy density E_{ac} for S-1D-M1 corresponding to different actuation voltages ranging from 26 to 103 V is found to be in the range 7 to 168 J/m^3 as presented in Table S2 in the Supplemental Material (Sec. S4). While simulating other configurations, since resulting pressure amplitudes at similar actuation voltages would be of the same order, a similar range of acoustic energy density values is used.

V. RESULTS AND DISCUSSION

We first present particle dynamics and trapping in the shaped traps. The time variation of particle position and velocity is presented and explained from the consideration of acoustic radiation force and the fluidic viscous force. We then report a general criterion for particle trapping based on the ratio of the acoustic energy to the fluidic viscous work (β), irrespective of the experimental condition. Further, we present the effect of the initial streamline, channel widths, chamber shape, standing-wave pattern, and harmonic modes, on the particle trajectory and the final trapping location. Also, we characterize the dimensionless location of the trapping site with parameter, β. Finally, we present a discussion on the comparison of the present device with the existing traditional S-BAW L-PRF trapping setups.

A. Particle dynamics and trapping under acoustic radiation force and fluid drag

Numerical simulation and experimental results of the dynamics and trapping of a particle of diameter, $D = 25$ μm in an S-1D-M1 trap of width 400 μm and length 750 μm at a flow rate, $Q = 15$ μl/min exposed to a 1D S-BAW operating at the first harmonic (half-wave) mode, M1 with $E_{ac} = 120$ J/m^3 are presented in Figs. 3 and 4, and Video S1 [58]. As observed from simulations and experiments, the particle after entering the chamber crosses the nodal plane, and finally gets trapped at an off-nodal position. The origin (0, 0) of the coordinate system is taken at the geometric center of the rectangular trapping chamber (see Fig. 1). The variation of the position (x, y) and velocity components (u,v) of the center of the particle as it traverses through the chamber, at a few important time instants (A to H), are depicted in Fig. 4. Experimentally, the velocity components are calculated using the instantaneous positions of the particle as it traverses. It is observed that after entering the chamber at time instant A, the particle translates along the y direction until instant B, as indicated by a sharp gradient in the y component of velocity (v), and then slows down. The particle further slows down after crossing the nodal plane at instant C and its direction of motion is reversed at instant E, marked by a negative y velocity. The magnitude of the negative y velocity slowly decreases and the particle tends to attain equilibrium beyond instant F and finally gets trapped at instant G. The trapped particle is released (instant H) by switching off the acoustic field. We find that the time variations of the particle positions and velocities obtained from the numerical simulations are in excellent agreement (within 5%) with that from our experiments, validating the numerical model. The successive pictures of particle motion in the case of other 1D shaped-trap configurations are presented in detail in Fig. S3 in the Supplemental Material (Sec. S6).

The dynamical motion of the particle can be explained by analyzing the relevant forces, namely the axial primary

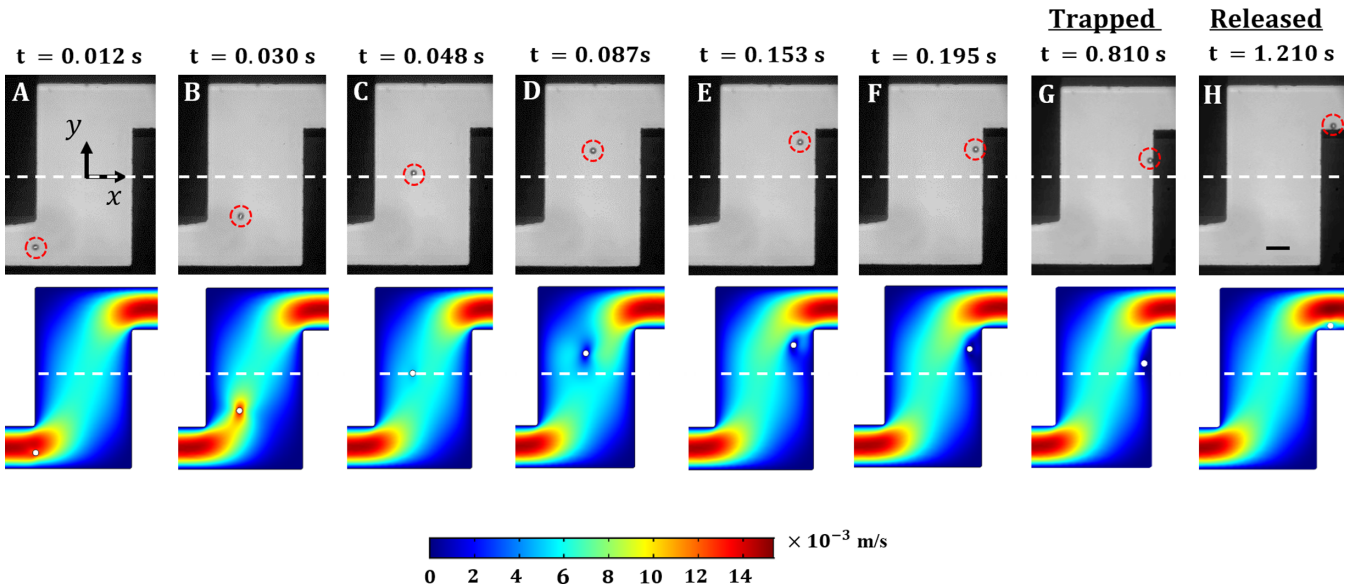

FIG. 3. Successive pictures (at important instants: A to H) of a microparticle's travel through an S-1D-M1 trapping chamber, predicted from our numerical simulations and experiments, with particle diameter $D = 25\ \mu$m, S-shaped trap of width 400 μm and length 750 μm, flow rate, $Q = 15\ \mu$l/min, 1D SW operating at the first harmonic (half-wave) mode, M1 with $E_{ac} = 120\text{J/m}^3$. The color legend refers to the magnitude of velocity in the computational domain in m/s. Scale bar represents 100 μm.

radiation force, $F_{A,}$ and the fluidic drag force, F_D acting on the particle as shown in Fig. 4(b). The procedure used for estimating F_A and F_D is presented in the Supplemental Material (Sec. S7). Once the particle enters the chamber at instant A, F_A acts on it in the flow direction supporting its motion, which explains the initial acceleration of the particle. Before crossing the pressure nodal plane at instant C, the acoustic force supports particle motion and therefore the ratio of the acoustic to fluid drag force is positive. In the case of a standing wave, A-PRF varies sinusoidally and is directed towards the nodal plane located at $y = 0$. In a half-wave scenario, the maximum A-PRF occurs at a distance of one-fourth of the chamber length along the wave direction from the walls. The particle crosses the location of maximum F_A at instant B, when it attains the maximum y-direction velocity (v), and beyond this instant, the ARF decreases, explaining the deceleration

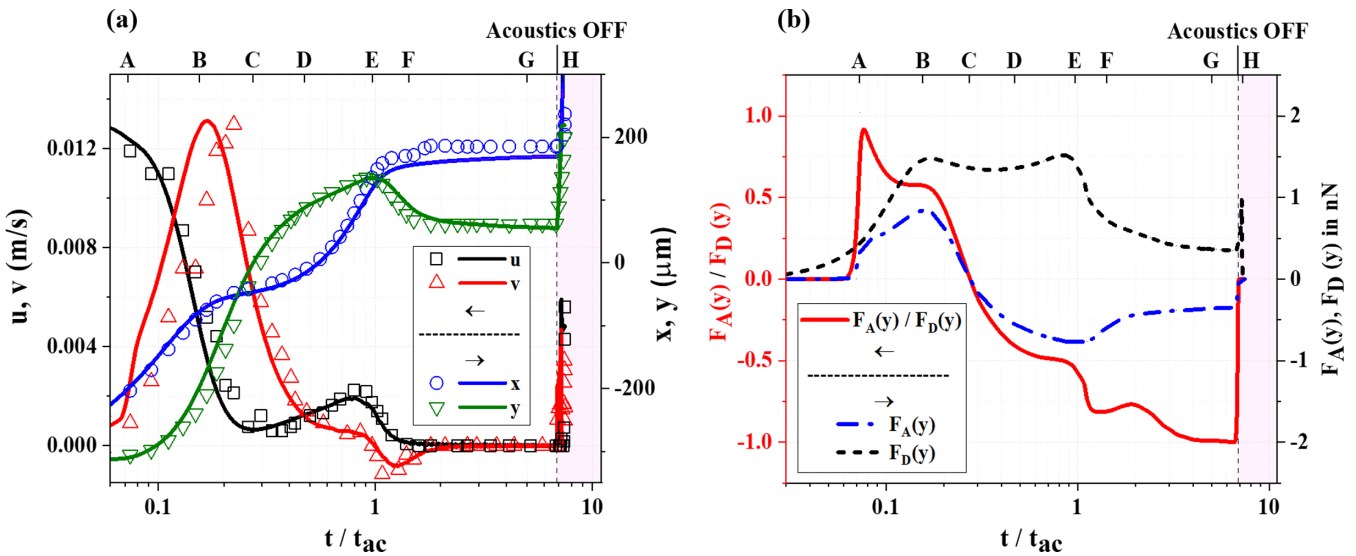

FIG. 4. (a) Time variation of location (x, y) and velocities (u,v) of a microparticle in the S-1D-M1 trapping chamber from our numerical simulations and experiments, (b) Time variation of A-PRF $F_A(y)$ and fluid drag force $F_D(y)$, and the ratio of the two forces, $F_A(y)/F_D(y)$, with particle diameter $D = 25\ \mu$m, S-shaped trap of width 400 μm and length 750 μm, flow rate $Q = 15\ \mu$l/min, 1D SW operating at the first harmonic (half-wave) mode, M1 with $E_{ac} = 120\ \text{J/m}^3$. Important instants ($A$ to H) in the particle's travel are marked in the plots for reference. Solid lines refer to simulation results. Symbols represent the experimental results. As marked in the figure, the vertical dashed line indicates the instant (H) at which acoustics is turned off. The shaded regions in both (a) and (b) represent the particle's travel after the acoustics is turned off. Time (t) has been nondimensionalized using the acoustophoretic timescale [62].

of the particle. At the nodal plane, $F_A = 0$ and the particle is simply dragged with the flow. Beyond the nodal plane, F_A is directed towards the nodal plane acting against the flow direction as indicated by a negative value of the force ratio after instant C and it gradually increases with an increase in the distance from the nodal plane. So, as the particle moves away from the nodal plane towards the outlet, it slows down. Since F_A always acts towards the nodal plane, particle trapping is possible only above the nodal plane where the ARF and fluidic drag force act in the opposite directions. At instant E, the ARF exceeds the drag force which explains a reversal in the direction of motion (referred to as a U-turn) towards the nodal plane.

The U-turn (instant D to F) of the particle is a consequence of the shape of the chamber combined with the typical sinusoidal variation of F_A along the wave direction. At the peak of the U-turn, at instant E, the y component of the velocity is zero and it becomes negative beyond this instant, indicating that the y coordinate of the final trapping location (y_{TL}) will always be below the peak. The x coordinate of the particle increases continuously with a decrease in the x velocity until crossing the nodal plane at instant C and then the x velocity increases again. This is primarily attributed to the S shape of the chamber which offers a slowly diverging and then converging flow section. A significant change in the x position of the particle occurs between the time instants D and E. After instant E, although the particle moves to a region of smaller fluid velocity closer to the wall, no significant change in the x position is observed. After completing the U-turn, beyond F, the particle proceeds to an increasingly stable configuration by moving closer to the wall and the nodal plane since the particle now requires a lesser value of the acoustic force to overcome the smaller fluid drag experienced. The competition between the acoustic force and the flow drag ultimately leads to a balance at instant G, giving rise to stable trapping. At the final trapped position, the value of the force ratio is found to be $|F_A(y)/F_D(y)| \approx 1$, indicating a force balance and the velocity components are also zero, thus satisfying the two conditions required for complete trapping. The trapped particle could be readily released by switching off the acoustic field as indicated by instant H. Depending on the operating parameters, the total duration of the entire trapping process varies from 0.5 to 2 s, out of which the particle spends at least 90% of the time above the nodal plane before reaching the final trapping location at instant G.

B. Generalization of trapping and nontrapping regimes in terms of the acoustic energy to viscous work ratio, β

In the previous section, we considered the two competing forces, the A-PRF, and the fluid drag force, to explain the particle-trapping phenomenon. However, the highly dynamic nature of these forces during the course of particle motion makes it difficult to characterize the system based on the forces. Therefore, we attempt to generalize the trapping phenomenon by considering the competition between the acoustic energy and the fluid viscous work involved in the process. In order to propose a general criterion for particle trapping, we performed extensive simulations using S- and U-shaped traps with 1D and 2D SW for the resonance modes M1 and M2, with variations in energy density (E_{ac}), flow rate (Q), particle diameter (D), and inlet (outlet) channel width (W_i), as presented in Table S1 in the Supplemental Material (Sec. S4). The upper limit of the particle radius (a) considered in our simulations corresponds to a particle radius to wavelength ratio, $a/\lambda < 0.1$, satisfying the Rayleigh limit. Our results show that irrespective of the geometry of the shaped traps (refer to Fig. 1) and operating conditions, the trapping and nontrapping regimes can be generalized in terms of the parameter, β. The regime plot shown in Fig. 5(a) describes the trapping and nontrapping regimes for S-1D-M1 trap. As described in Sec. II, acoustic energy (E_A) and the viscous work (W_v) are nondimensionalized using the incoming kinetic energy of the particle, and their dimensionless forms (E_A^*, W_v^*) are considered to study the regimes. The shaded and unshaded regions represent the trapping and nontrapping regimes, respectively. The experimental data points pertaining to the trapped and nontrapped cases, indicated by hollow circular and triangular symbols, respectively, in Fig. 5(a) are in good agreement with the simulation results in demarcating the two regimes. Experimental images for particle trapping across various sizes, 15, 20, 25, and 36 μm, and successive pictures of trapping and nontrapping cases are shown in Fig. 5(b). Across the particle sizes considered in the simulations and experiments, the characterization of regimes and hence the critical value of β (β_{cr}) is found to be consistent. The slope of the demarcating line as shown in Fig. 5(a) is $\beta_{cr} = 4$, so for $\beta \geqslant 4$, and for $\beta < 4$, particle trapping and nontrapping regime, respectively, are observed for the S,U-1D-M1 case. Similarly, for the case of S,U-1D-M2, S,U-2D-M1, and U-2D-M2, the regime study shows a similar trend with $\beta_{cr} \approx 3.5$, 8.5, and 29, respectively (see Fig. 8). The reason that β_{cr} is different for different configurations may be attributed to the different near-trap velocity fields present in various configurations. Among all the configurations for which the regime study is carried out, since the trapping zone for the case of U-2D-M2 is closest [refer to Fig. 6(b)] to the inlet channel, comparatively higher velocities are present in the near-trap region which explain the requirement of higher acoustic energy to trap the particle, and thus higher β_{cr} (=29) (see Fig. 8).

C. Effect of the shaped-trap geometry and operating conditions on the particle trajectory and trapping location

The effect of geometry and dimensions of the shaped traps, the standing-wave patterns, and the resonance modes on the particle trajectory and final trapping location is presented in Fig. 6. Operating conditions corresponding to Fig. 6(a) are particle size $D = 25$ μm, energy density, $E_{ac} = 80$ J/m^3, and flow rate, $Q = 15$ μl/min, and those to Fig. 6(b) are particle size $D = 30$ μm, energy density $E_{ac} = 35$ J/m^3, and flow rate $Q = 7$ μl/min. Two different geometries of the shaped traps, namely S shaped and U shaped, are considered (see Fig. 1) with 1D and 2D SW in resonance modes M1, M2, and M3. The widths of the inlet and outlet channels are varied from 100 to 200 μm, and three different initial particle streamline positions are considered. The effect of variation in initial particle streamline position is explained via experimental trajectories TR1 to TR4 as shown in Fig. 6(a),

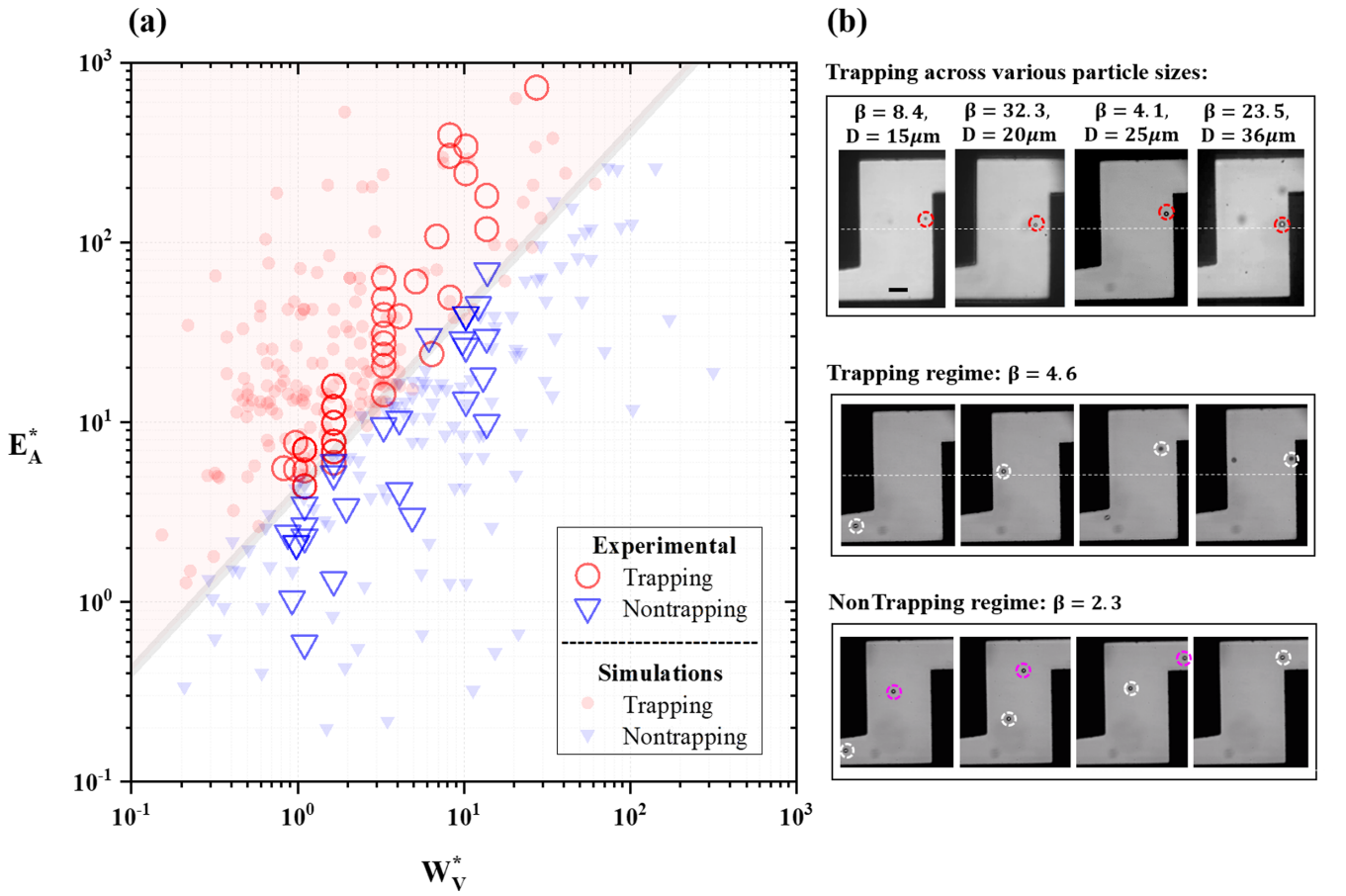

FIG. 5. (a) Generalization of trapping and nontrapping regimes in terms of the parameter β. The simulation data correspond to S,U-1D shaped traps with half-wave mode, M1, as indicated in Fig. 1 for a range of particle sizes, inlet channel width, flow rates, and acoustic energy densities; the simulation and experimental data are indicated using different symbols. The critical ratio $\beta_{cr} = 4$ is the slope of the demarcating line between the regimes. (b) For the case of S-1D-M1, experimental images are shown for particle trapping across various sizes, 15, 20, 25, and 36 μm encircled in red color, and also shown are the successive pictures of trapping ($\beta = 4.6$) and nontrapping ($\beta = 2.3$) cases for 25-μm particle size. For the nontrapping case, two particles (pink and white encircled) dominated by the viscous drag are shown while traveling in and out of the chamber. Scale bar represents 100 μm.

which is a result of the combination of overlaid images from four different experimental datasets at identical operating conditions. The effect of standing-wave pattern, resonance mode, and shaped-trap geometry is explained via trajectories TR5 to TR12 [Fig. 6(b)] from simulation. Variation in the operating parameters across various shaped-trap configurations leads to a choice of trapping site along the corresponding trapping zones as shown in Fig. 6(b). The effect of variation in the inlet and outlet channel width is explained in the Supplemental Material (Sec. S8) via trajectories TR13 to TR17.

For a 1D standing wave in half-wave mode M1 and a fixed geometry of the shaped trap, by comparing the trajectories TR1, TR2, TR3, and TR4, we observe that the initial particle streamline, although it affects the particle trajectory, does not alter the final trapping location (TL1) since the final trapping location is a location of zero net force which remains unaltered for different initial particle position and same operating conditions. We find that a particle moving closer to the upper wall of the inlet channel (TR1) executes a longer U-turn to reach TL1 and hence takes more time as compared to the one in TR3 and TR4, also confirmed by experimental snapshots (see insets in Fig. 8).

At a fixed experimental condition, compared to the S-shaped trap, the use of a U-shaped trap reveals a different particle trajectory as seen from a comparison of the trajectories TR4 and TR5 and causes a horizontal shift in the final trapping location towards the left from TL1 to TL2. Since S- and U- shaped chambers have similar force fields below the nodal plane, therefore the particle trajectories in the two cases overlap up to the nodal plane and deviate beyond that. The trapping location in a U-shaped trap is mirrored about the vertical centerline of the trapping chamber compared to the S-shaped trap.

It is observed that at a fixed experimental condition for mode M1, in the case of both S- and U-shaped traps, compared to a 1D actuation case, the use of a 2D resonating cavity alters the particle trajectory from TR4 to TR6 and TR5 to TR7, respectively, as well as the final trapping location from TL1 to TL3 and TL2 to TL4, respectively. The final trapping location in case of 2D resonance cavity shifts laterally towards the 2D chamber wall along the x direction. In the 2D S- and U-shaped traps, owing to the characteristic acoustic force fields [Figs. 7(d)–7(f)], the reversal in the direction of the particle motion observed is different from that in the case of

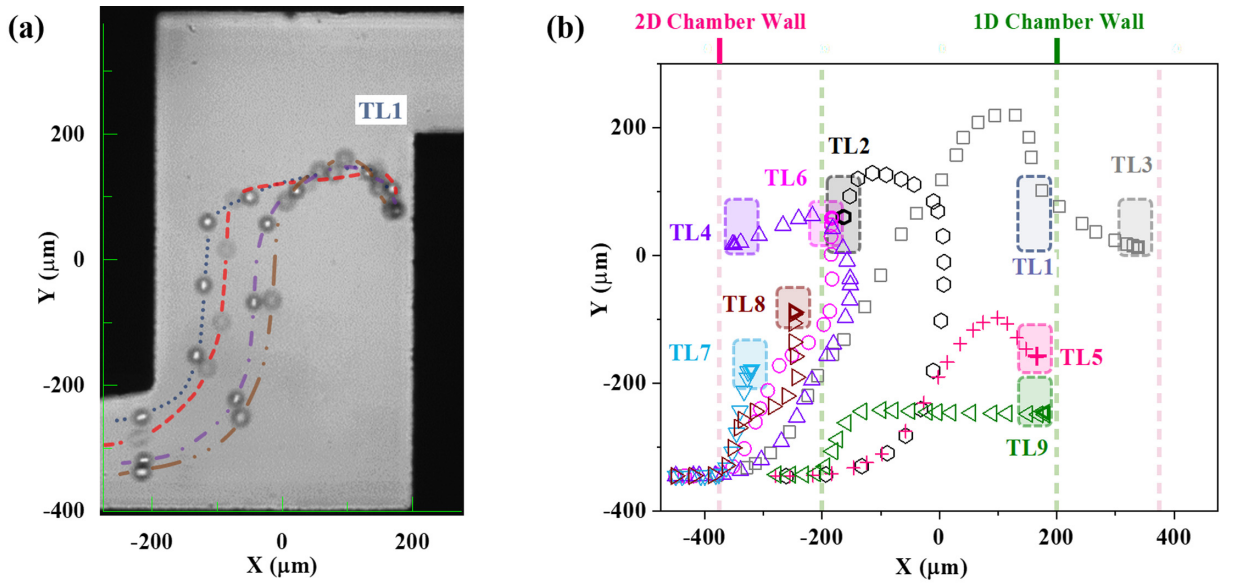

Legend				
Configuration	S-1D-M1 (Experimental)			
Trajectory	TR1	TR2	TR3	TR4
Trapping Location	TL1			
Initial y location (μm)	-264	-288	-316	-331

⬡	□	△	+	○	▽	▷	◁
U-1D-M1	S-2D-M1	U-2D-M1	S,U-1D-M2	S-2D-M2	U-2D-M2	S,U-2D-M3	S,U-1D-M3
TR5	TR6	TR7	TR8	TR9	TR10	TR11	TR12
TL2	TL3	TL4	TL5	TL6	TL7	TL8	TL9
-345							

FIG. 6. Particle trajectories and final trapping locations for different shaped traps. Please refer to legends in the respective tables for detailed information. (a) shows the effect of variation in initial particle streamline position explained via overlaid images from four different experimental datasets, leading to trajectories TR1 to TR4. Operating conditions are particle size $D = 25\ \mu$m, energy density $E_{ac} = 80\ \mathrm{J/m^3}$, and flow rate $Q = 15\ \mu$l/min, and (b) shows the effect of standing-wave pattern, resonance mode, and shaped trap geometry explained via trajectories TR5 to TR12. Operating conditions are particle size $D = 30\ \mu$m, energy density $E_{ac} = 35\ \mathrm{J/m^3}$, and flow rate $Q = 7\ \mu$l/min. Shaded regions around various trapping locations indicate the zones containing possible trapping sites for different particle sizes, flow rates, and energy densities in the range studied. The vertical dashed lines represent walls of 1D and 2D chambers as labeled in (b).

1D actuated traps. We notice that in the half-wave mode M1, the trapping location is always beyond the nodal plane in the upper half of the trapping chamber, so we study the effect of higher resonance modes on the particle-trapping location.

In both S- and U- shaped traps with both 1D and 2D resonance, by using resonance mode M2 and M3, we could achieve trapping locations TL5, TL7, TL8, and TL9 in the lower half of the chamber closer to the channel inlet region via trajectories TR8, TR10, TR11, and TR12, respectively, thus significantly modifying the y coordinate of the final trapping location [Fig. 6(b)]. TL6 in the case of S-2D-M2, as an exception, is found to be situated at a relatively farther y coordinate and not in the lower half of the chamber. This could be attributed to a near-zero acoustic pressure and very low acoustic force region near the inlet inside the chamber as shown in Fig. 7(e), which makes the particle follow (TR9) the dominating flow field in the near-inlet region and hence getting captured (TL6) away from it. For higher-resonance

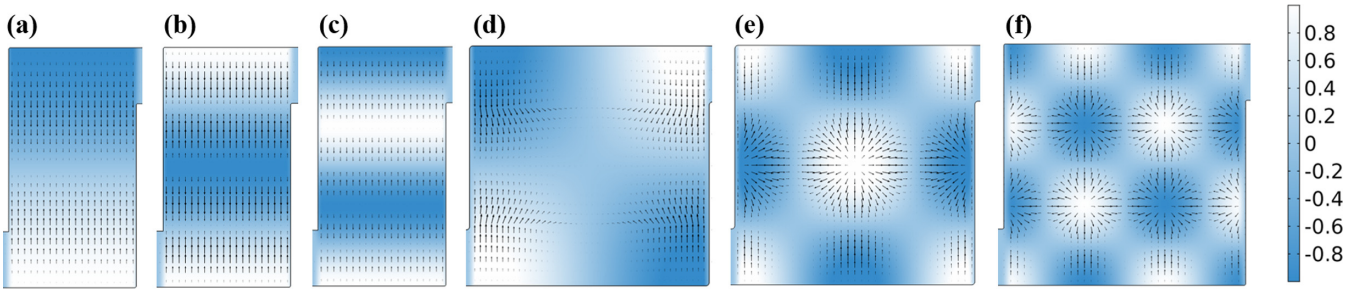

FIG. 7. Acoustic radiation force field is shown via arrow plots with acoustic pressure field in the background, for S-1D-M1 (a), S-1D-M2 (b), S-1D-M3 (c), S-2D-M1 (d), S-2D-M2 (e), and S-2D-M3 (f). The length and the direction of the arrows signify the magnitude and direction of the net acoustic radiation force acting on a particle. The scale shows the magnitude of dimensionless acoustic pressure (p_1/p_a). The color corresponding to the extremes and middle of the scale bar signify pressure antinodal, and pressure nodal regions, respectively. The length of arrows across (a) to (f) are not to scale.

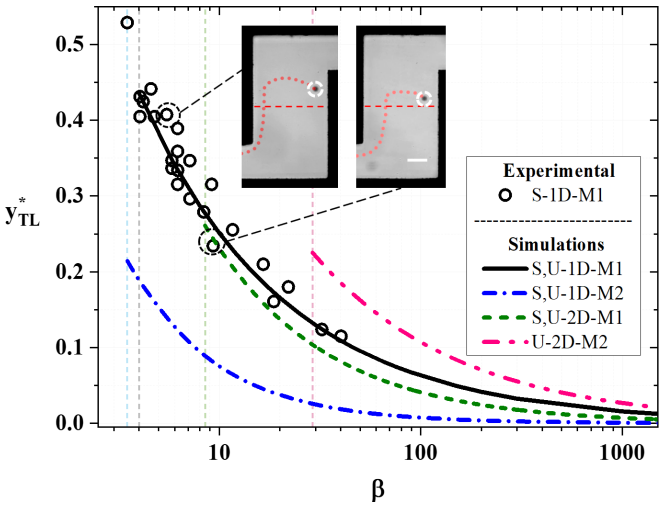

FIG. 8. The variation of the dimensionless distance of the trapping location from the pressure nodal plane or region in the y direction, i.e., y^*_{TL} with the parameter β for the case of S,U-1D and S,U-2D chambers with resonance modes M1 and M2. Dashed vertical lines indicate the β_{cr} for respective configurations. Insets qualitatively reveal the effect of β on y^*_{TL}.

modes, since trapping location is far from the outlet, hence the shape of the trap has little effect on the trapping phenomenon; therefore, the trajectories TR8, TR12, and TR11 and trapping locations TL5, TL9, and TL8, respectively, are similar for the case of S- and U-shaped traps, as seen in the cases with mode M2 for 1D, M3 for 1D, and M3 for 2D chambers, respectively. Although higher-resonance modes across different-shaped traps are found to offer a variety of trapping sites (TL5–9), the combined effect of the peculiar acoustic force fields [Figs. 7(d)–7(f)] and the corresponding flow fields that the particle is exposed to makes trapping trajectories and trapping sites less predictable in the case of 2D resonance cavities.

Integral to the studies of particle trajectory and trapping sites are the acoustic pressure variations inside the resonating cavities. The acoustic pressure variation akin to the incoming pressure field given by Eq. (5) is plotted in Fig. 7. The acoustic radiations forces calculated by Eqs. (6)–(9) for each case as shown in Fig. 7 are plotted via arrows with the acoustic pressure field surface in the background. Pressure nodal and antinodal, planes in the case of 1D chambers, and regions in the case of 2D chambers with resonance modes M1, M2, and, M3 can be seen in Figs. 7(a)–7(f), respectively. The particles traveling through respective chambers are exposed to the acoustic force field and the corresponding flow field. As described in the previous subsections, the particle under favorable conditions looks for the zero net force region and gets trapped at a suitable trapping location depending on the competing effects inside the chamber as described in Fig. 8.

Irrespective of the geometry of the shaped trap and experimental condition, the variation in the y coordinate of the trapping location y_{TL} is found to be a function of the parameter β as presented in Fig. 8. Experimental results for S-1D-M1 are found to have a good agreement with the simulations. Here, y_{TL} is nondimensionalized with $y_0 = (\lambda/8)$, which in the 1D case is the distance from the nodal plane (nearest to the trapping site) to the plane at which the A-PRF attains its maximum magnitude. Since trapping or nontrapping of a particle inside the chamber is decided over a length of y_0, therefore it is taken as a characteristic length to obtain $y^*_{TL} = y_{TL}/y_0$. Although there are no distinct nodal planes in the case of 2D chambers, from Figs. 7(d)–7(f) it is found that the characteristic length scale over which trapping occurs in 2D chambers is not very different from y_0 and hence we choose y_0 as the characteristic length scale across all configurations. We find that y^*_{TL} varies with β following the relation, $y^*_{TL} \sim \beta^{-c}$, with exponent c varying from 0.6 to 1.0. The relationship between y^*_{TL} and β confirms that higher acoustic energy or lower viscous work leads to a trapping location closer to the pressure nodal plane or region. As shown in insets of Fig. 8, with decreasing β, the trapping location is shifted further away from the nodal plane until it attains a critical value β_{cr}, beyond which particle trapping is not possible. For 1D chambers, we find $y^*_{TL} = 1.0\,\beta^{-0.6}$ with a goodness of fit $R^2 = 0.93$ for S,U-1D-M1, and $y^*_{TL} = 0.75\,\beta^{-1.0}$ with $R^2 = 0.921$ for S,U-1D-M2. For 2D chambers, we find $y^*_{TL} = 1.3\,\beta^{-0.75}$ with a goodness of fit $R^2 = 0.923$ for S,U-2D-M1, and $y^*_{TL} = 1.7\,\beta^{-0.6}$ with $R^2 = 0.94$ for U-2D-M2. The values of β_{cr} for S,U-1D-M1, S,U-1D-M2, S,U-2D-M1, and U-2D-M2 are found to be 4, 3.5, 8.5, and 29, respectively.

From the above studies, we conclude that for the fundamental resonance mode M1, the geometry of the shaped trap (S- or U configuration) and the standing-wave pattern (1D or 2D) has a significant effect on the x coordinate of the final trapping location. For the case of higher harmonics, this effect on the x coordinate is more dominant with the change in the standing-wave pattern as compared to the change in geometry of the shaped trap. Similarly, the y coordinate of the final trapping location (y_{TL}) markedly varies with the resonance mode and can also be controlled by varying the ratio of the acoustic energy to viscous work, following the relation $y^*_{TL} \sim \beta^{-c}$. The parameter β can be modified by varying the acoustic energy density, particle size, particle, and medium properties, and the flow rate to provide a different y_{TL}. Therefore, by suitably selecting the chamber shape, actuation pattern, resonance mode, particle-fluid combination, and adjusting the parameter β, a suitable trapping location can be chosen from a zone of possible trapping sites shown in Fig. 6(b). The trapping sites can be used for trapping multiple particles or controlling the trapping location of a single particle inside the chamber.

D. Comparison between A-PRF and L-PRF

Previously reported traditional BAW microfluidic trapping platforms [3,10,46,47] utilizing the L-PRF as the main retention force measured the maximum retention force in the range 0.002–0.5 nN for a single particle in the size range of 10–12 μm operating at a frequency range of 2.5–12.4 MHz. Taking advantage of high lateral gradients in the velocity field present over the transducer area, these trapping systems are generally designed to trap particle clusters laterally against the flow. The increased dominance of drag force over L-PRF renders trapping of single particle difficult as compared to a cluster, which could be attributed to a more exposed surface area to volume ratio [48] in case of a single particle and the inferior

size dependency of the retention force, L-PRF ($\sim a^2$) [43,59] as compared to the A-PRF ($\sim a^3$). Based on the experimental findings, the current work utilizing the A-PRF as the main retention force shows a significant increase in the maximum retention force. For a single particle in the size range 15−36 μm for a frequency range of 1−2 MHz, the retention force is found to be on the order 1−10 nN. Moreover, the maximum retention force for a particle size as low as 12 μm, trapped at a fluid velocity of 12 mm/s with a resonating frequency of 13 MHz, is found to be 3.25 nN as shown in the Supplemental Material (Sec. S9), which is at least one order of magnitude higher for similar parameters as reported in the literature [3,10,46,47]. Stronger size dependency of A-PRF is found to produce a retention force in the range 2.5 to 20 nN for larger particle size ($\sim$25−36 μm) even at low-frequency (1–3-MHz) operation. Furthermore, with suitable design modifications such as better chamber design and higher-frequency operation utilizing multinodal resonance, an improved device could yield an even more promising setup for trapping single particles or high-efficiency particle cluster traps.

VI. CONCLUSION

In this study, we have presented axial primary radiation force (A-PRF) driven acoustic trapping of microparticles in 1D and 2D microfluidic shaped traps exposed to standing bulk acoustic waves (S-BAW) in the fundamental resonance mode and higher harmonics using numerical simulations and experiments. The described acoustic trapping mechanism emphasizes the importance of utilizing the A-PRF which originates from the more dominant potential energy gradients present away from the nodal plane, unlike the lateral primary radiation force (L-PRF) which relies on the smaller lateral acoustic velocity field gradients effective only near the pressure nodal plane. This results in a higher retention force allowing the trapping of particles over a wider range of operating conditions.

We show that the particle trapping is governed by a competition between the A-PRF and viscous drag. The particle-trapping and nontrapping regimes were characterized in terms of the ratio of the acoustic energy to the viscous work, β. For 1D trapping chambers in the fundamental resonance mode, the critical value of the parameter β is seen to be $\beta_{cr} = 4.0$; hence, particle trapping is observed for $\beta \geqslant 4.0$, and the nontrapping for $\beta < 4.0$. The critical value of the parameter β is obtained and reported for other trapping configurations also. For a fixed resonance mode, particle trajectory depends on the chamber shape, standing-wave pattern, and initial streamline position but is independent of the inlet channel width. The final trapping location along the chamber length in case of both 1D and 2D S-BAW is found to be a function of the parameter β following $y^*_{\mathrm{TL}} \sim \beta^{-c}$, with the exponent c ranging from 0.6 to 1.0, varying with the resonance mode and standing-wave pattern. We found an excellent agreement between the numerical simulations and experimental results. Precise control over the particle-trapping site location was achieved in the current system as a key improvement over the existing trapping systems. By varying the chamber shape, standing-wave pattern, resonance modes, and the parameter β, it is possible to achieve a wide range of trapping locations inside the chamber.

Our study not only provides a fundamental understanding of acoustic trapping of particles in shaped traps, it also offers ways for controlling the final trapping location, creating a zone of trapping sites. The presented way of capturing particles or cells could open up the route to upscale the existing perfusion-based cell-handling unit operations. The stronger axial primary radiation force is more promising and could potentially enable very high retention forces scaling up the throughput rate, which could be an important contribution to the field of particle and cell trapping, finding applications in the development of parallel or sequential high-throughput trapping devices for biochemical assays.

ACKNOWLEDGMENTS

A.K.S. thanks the Department of Science & Technology (DST), Government of India for providing financial support in the form of the Swarnajayanti Fellowship Award via Grant No. DST/SJF/ETA-03/2017-18. The support from the Indian Institute of Technology Madras to the Micro Nano Bio Fluidics Group under the funding for Institutions of Eminence scheme of Ministry of Education, Government of India [Sanction No. 11/9/2019-U.3(A)] is also acknowledged. The authors acknowledge the support of CNNP, IIT Madras for the device fabrication. L.M. thanks D. Harsha, S. K. Jain, N. S. Satpathi, and S. Z. Hoque for helping with the fabrication and simulations.

[1] T. Laurell, F. Petersson, and A. Nilsson, Chip integrated strategies for acoustic separation and manipulation of cells and particles, Chem. Soc. Rev. **36**, 492 (2007).

[2] J. V. Norris, M. Evander, K. M. Horsman-Hall, J. Nilsson, T. Laurell, and J. P. Landers, Acoustic differential extraction for forensic analysis of sexual assault evidence, Anal. Chem. **81**, 6089 (2009).

[3] M. Evander, L. Johansson, T. Lilliehorn, J. Piskur, M. Lindvall, S. Johansson, M. Almqvist, T. Laurell, and J. Nilsson, Noninvasive acoustic cell trapping in a microfluidic perfusion system for online bioassays, Anal. Chem. **79**, 2984 (2007).

[4] A. Lenshof, M. Evander, T. Laurell, and J. Nilsson, Acoustofluidics 5: Building microfluidic acoustic resonators, Lab Chip **12**, 684 (2012).

[5] H. Bruus, Acoustofluidics 7: The acoustic radiation force on small particles, Lab Chip **12**, 1014 (2012).

[6] P. B. Muller, M. Rossi, A. G. Marín, R. Barnkob, P. Augustsson, T. Laurell, C. J. Kähler, and H. Bruus, Ultrasound-induced acoustophoretic motion of microparticles in three dimensions, Phys. Rev. E **88**, 023006 (2013).

[7] T. Lilliehorn, U. Simu, M. Nilsson, M. Almqvist, T. Stepinski, T. Laurell, J. Nilsson, and S. Johansson, Trapping of microparticles in the near field of an ultrasonic transducer, Ultrasonics **43**, 293 (2005).

[8] B. Hammarström, M. Evander, H. Barbeau, M. Bruzelius, J. Larsson, T. Laurell, and J. Nilsson, Non-contact acoustic cell trapping in disposable glass capillaries, Lab Chip **10**, 2251 (2010).

[9] H. M. Hertz, Standing-wave acoustic trap for nonintrusive positioning of microparticles, J. Appl. Phys. **78**, 4845 (1995).

[10] J. Svennebring, O. Manneberg, P. Skafte-Pedersen, H. Bruus, and M. Wiklund, Selective bioparticle retention and characterization in a chip-integrated confocal ultrasonic cavity, Biotechnol. Bioeng. **103**, 323 (2009).

[11] A. Nath and A. K. Sen, Acoustic Behavior of a Dense Suspension in an Inhomogeneous Flow in a Microchannel, Phys. Rev. Appl. **12**, 054009 (2019).

[12] A. Nath, L. Malik, and A. K. Sen, Combined acoustic relocation and acoustophoretic migration for particle transfer between coflowing fluids in a microchannel, Phys. Rev. Fluids **6**, 044201 (2021).

[13] D. Baresch, J.-L. Thomas, and R. Marchiano, Observation of a Single-Beam Gradient Force Acoustical Trap for Elastic Particles: Acoustical Tweezers, Phys. Rev. Lett. **116**, 024301 (2016).

[14] A. Riaud, M. Baudoin, O. Bou Matar, L. Becerra, and J.-L. Thomas, Selective Manipulation of Microscopic Particles with Precursor Swirling Rayleigh Waves, Phys. Rev. Appl. **7**, 024007 (2017).

[15] M. Baudoin, J. L. Thomas, R. Al Sahely, J. C. Gerbedoen, Z. Gong, A. Sivery, O. B. Matar, N. Smagin, P. Favreau, and A. Vlandas, Spatially selective manipulation of cells with single-beam acoustical tweezers, Nat. Commun. **11**, 1 (2020).

[16] J. Shi, D. Ahmed, X. Mao, S. C. S. Lin, A. Lawit, and T. J. Huang, Acoustic tweezers: Patterning cells and microparticles using standing surface acoustic waves (SSAW), Lab Chip **9**, 2890 (2009).

[17] Z. Ma, K. Melde, A. G. Athanassiadis, M. Schau, H. Richter, T. Qiu, and P. Fischer, Spatial ultrasound modulation by digitally controlling microbubble arrays, Nat. Commun. **11**, 1 (2020).

[18] S. Karthick, P. N. Pradeep, P. Kanchana, and A. K. Sen, Acoustic impedance-based size-independent isolation of circulating tumour cells from blood using acoustophoresis, Lab Chip **18**, 3802 (2018).

[19] K. Melde, A. G. Mark, T. Qiu, and P. Fischer, Holograms for acoustics, Nature (London) **537**, 518 (2016).

[20] A. Marzo and B. W. Drinkwater, Holographic acoustic tweezers, Proc. Natl. Acad. Sci. U.S.A. **116**, 84 (2019).

[21] I. Leibacher, P. Reichert, and J. Dual, Microfluidic droplet handling by bulk acoustic wave (BAW) acoustophoresis, Lab Chip **15**, 2896 (2015).

[22] J. Lee, S. Teh, A. Lee, H. H. Kim, C. Lee, and K. Shung, Transverse acoustic trapping using a gaussian focused ultrasound, Ultrasound. Med. Biol. **36**, 350 (2010).

[23] A. Fornell, C. Johannesson, S. S. Searle, A. Happstadius, J. Nilsson, and M. Tenje, An acoustofluidic platform for non-contact trapping of cell-laden hydrogel droplets compatible with optical microscopy, Biomicrofluidics **13**, 044101 (2019).

[24] J. Nilsson, M. Evander, B. Hammarström, and T. Laurell, Review of cell and particle trapping in microfluidic systems, Anal. Chim. Acta **649**, 141 (2009).

[25] O. Manneberg, B. Vanherberghen, J. Svennebring, H. M. Hertz, B. Önfelt, and M. Wiklund, A three-dimensional ultrasonic cage for characterization of individual cells, Appl. Phys. Lett. **93**, 1 (2008).

[26] M. Wiklund and H. M. Hertz, Ultrasonic enhancement of bead-based bioaffinity assays, Lab Chip **6**, 1279 (2006).

[27] D. Bazou, R. Kearney, F. Mansergh, C. Bourdon, J. Farrar, and M. Wride, Gene expression analysis of mouse embryonic stem cells following levitation in an ultrasound standing wave trap, Ultrasound Med. Biol. **37**, 321 (2011).

[28] J. Hultström, O. Manneberg, K. Dopf, H. M. Hertz, H. Brismar, and M. Wiklund, Proliferation and viability of adherent cells manipulated by standing-wave ultrasound in a microfluidic chip, Ultrasound Med. Biol. **33**, 145 (2007).

[29] C. P. Clark, K. Xu, O. Scott, J. Hickey, A. C. Tsuei, K. Jackson, and J. P. Landers, Acoustic trapping of sperm cells from mock sexual assault samples, Forensic Sci. Int. Genet. **41**, 42 (2019).

[30] J. Liu, L. A. Kuznetsova, G. O. Edwards, J. Xu, M. Ma, W. M. Purcell, S. K. Jackson, and W. T. Coakley, Functional three-dimensional HepG2 aggregate cultures generated from an ultrasound trap: Comparison with HepG2 spheroids, J. Cell. Biochem. **102**, 1180 (2007).

[31] A. Haake, A. Neild, G. Radziwill, and J. Dual, Positioning, displacement, and localization of cells using ultrasonic forces, Biotechnol. Bioeng. **92**, 8 (2005).

[32] B. Vanherberghen, O. Manneberg, A. Christakou, T. Frisk, M. Ohlin, H. M. Hertz, B. Önfelt, and M. Wiklund, Ultrasound-controlled cell aggregation in a multi-well chip, Lab Chip **10**, 2727 (2010).

[33] J. Sinclair, J. Pihl, J. Olofsson, M. Karlsson, K. Jardemark, D. T. Chiu, and O. Orwar, A cell-based bar code reader for high-throughput screening of ion channel-ligand interactions, Anal. Chem. **74**, 6133 (2002).

[34] A. F. Sarioglu, N. Aceto, N. Kojic, M. C. Donaldson, M. Zeinali, B. Hamza, A. Engstrom, H. Zhu, T. K. Sundaresan, D. T. Miyamoto, X. Luo, A. Bardia, B. S. Wittner, S. Ramaswamy, T. Shioda, D. T. Ting, S. L. Stott, R. Kapur, S. Maheswaran, D. A. Haber, and M. Toner, A microfluidic device for label-free, physical capture of circulating tumor cell clusters, Nat. Methods **12**, 685 (2015).

[35] J. Voldman, Electrical forces for microscale cell manipulation, Annu. Rev. Biomed. Eng. **8**, 425 (2006).

[36] M. A. M. Gijs, Magnetic bead handling on-chip: New opportunities for analytical applications, Microfluid. Nanofluid. **1**, 22 (2004).

[37] A. Ashkin, Optical trapping and manipulation of neutral particles using lasers, Proc. Natl. Acad. Sci. U.S.A. **94**, 4853 (1997).

[38] I. Leibacher, P. Hahn, and J. Dual, Acoustophoretic cell and particle trapping on microfluidic sharp edges, Microfluid. Nanofluid. **19**, 923 (2015).

[39] X. Xu, Z. Li, and A. Nehorai, Finite element simulations of hydrodynamic trapping in microfluidic particle-trap array systems, Biomicrofluidics **7**, 054108 (2013).

[40] J. Voldman, M. Toner, M. L. Gray, and M. A. Schmidt, Design and analysis of extruded quadrupolar dielectrophoretic traps, J. Electrostat. **57**, 69 (2003).

[41] S. K. Jain, U. Banerjee, and A. K. Sen, Trapping and coalescence of diamagnetic aqueous droplets using negative magnetophoresis, Langmuir **36**, 5960 (2020).

[42] A. Blázquez-Castro, Optical tweezers: Phototoxicity and thermal stress in cells and biomolecules, Micromachines **10**, 1 (2019).

[43] M. Evander and J. Nilsson, Acoustofluidics 20: Applications in acoustic trapping, Lab Chip **12**, 4667 (2012).

[44] J. F. Spengler and W. T. Coakley, Ultrasonic trap to monitor morphology and stability of developing microparticle aggregates, Langmuir **19**, 3635 (2003).

[45] B. Hammarström, T. Laurell, and J. Nilsson, Seed particle-enabled acoustic trapping of bacteria and nanoparticles in continuous flow systems, Lab Chip **12**, 4296 (2012).

[46] P. Glynne-Jones, C. E. M. Démoré, C. Ye, Y. Qiu, S. Cochran, and M. Hill, Array-controlled ultrasonic manipulation of particles in planar acoustic resonator, IEEE Trans. Ultrason. Ferroelectr. Freq. Control **59**, 1258 (2012).

[47] I. Gralinski, S. Raymond, T. Alan, and A. Neild, Continuous flow ultrasonic particle trapping in a glass capillary, J. Appl. Phys. **115**, 054505 (2014).

[48] S. M. Woodside, B. D. Bowen, and J. M. Piret, Measurement of ultrasonic forces for particle-liquid separations, AlChE J. **43**, 1727 (1997).

[49] T. Lilliehorn, M. Nilsson, U. Simu, S. Johansson, M. Almqvist, J. Nilsson, and T. Laurell, Dynamic arraying of microbeads for bioassays in microfluidic channels, Sens. Actuators B **106**, 851 (2005).

[50] O. Manneberg, B. Vanherberghen, B. Önfelt, and M. Wiklund, Flow-free transport of cells in microchannels by frequency-modulated ultrasound, Lab Chip **9**, 833 (2009).

[51] S. M. Hagsäter, T. G. Jensen, H. Bruus, and J. P. Kutter, Acoustic resonances in microfluidic chips: Full-image micro-PIV experiments and numerical simulations, Lab Chip **7**, 1336 (2007).

[52] C. R. P. Courtney, C. K. Ong, B. W. Drinkwater, A. L. Bernassau, P. D. Wilcox, and D. R. S. Cumming, Manipulation of particles in two dimensions using phase controllable ultrasonic standing waves, Proc. R. Soc. A: Math., Phys. Eng. Sci. **468**, 337 (2012).

[53] M. Wiklund, S. Nilsson, and H. M. Hertz, Ultrasonic trapping in capillaries for trace-amount biomedical analysis, J. Appl. Phys. **90**, 421 (2001).

[54] M. Kim, P. V. Bayly, and J. M. Meacham, Motile cells as probes for characterizing acoustofluidic devices, Lab Chip **21**, 521 (2021).

[55] J. S. Bach and H. Bruus, Theory of acoustic trapping of microparticles in capillary tubes, Phys. Rev. E **101**, 023107 (2020).

[56] L. P. Gorkov, On the forces acting on a small particle in an acoustical field in an ideal fluid, Sov. Phys.–Dokl. **6**, 773 (1962).

[57] R. Barnkob and H. Bruus, Acoustofluidics: Theory and simulation of radiation forces at ultrasound resonances in microfluidic devices, Proc. Mtgs. Acoust. **6**, 020001 (2009).

[58] See Supplemental Material at http://link.aps.org/supplemental/10.1103/PhysRevE.105.035103 for the derivation of acoustic radiation force in the case of two-dimensional resonance, scaling of secondary and streaming forces, comparison of streaming and bulk fluid velocity fields, range of relevant parameters and properties of fluid and solid medium, mesh convergence study, particle trapping in other shaped trap configurations, method of estimation of forces in the trapping phenomenon, effect of inlet (outlet) channel width on particle trajectory and trapping location, higher-frequency operation of the trapping device, and a video of the trapping phenomenon.

[59] M. Groschl, Ultrasonic separation of suspended particles - Part I: Fundamentals, Acustica **84**, 432 (1998).

[60] S. Z. Hoque, A. Nath, and A. K. Sen, Dynamical motion of a pair of microparticles at the acoustic pressure nodal plane under the combined effect of axial primary radiation and interparticle forces, J. Acoust. Soc. Am. **150**, 307 (2021).

[61] M. Wiklund, R. Green, and M. Ohlin, Acoustofluidics 14: Applications of acoustic streaming in microfluidic devices, Lab Chip **12**, 2438 (2012).

[62] H. Bruus, Acoustofluidics 10: Scaling laws in acoustophoresis, Lab Chip **12**, 1578 (2012).

[63] P. Augustsson, J. T. Karlsen, H. W. Su, H. Bruus, and J. Voldman, Iso-acoustic focusing of cells for size-insensitive acousto-mechanical phenotyping, Nat. Commun. **7**, 1 (2016).

[64] H. Bruus, Acoustofluidics 1: Governing equations in microfluidics, Lab Chip **11**, 3742 (2011).

[65] H. Bruus, Acoustofluidics 2: Perturbation theory and ultrasound resonance modes, Lab Chip **12**, 20 (2012).

[66] J. Donea, S. Giuliani, and J. P. Halleux, An arbitrary Lagrangian-Eulerian finite element method for transient dynamic fluid-structure interactions, Comput. Methods Appl. Mech. Eng. **33**, 689 (1982).

[67] R. Barnkob, P. Augustsson, T. Laurell, and H. Bruus, Measuring the local pressure amplitude in microchannel acoustophoresis, Lab Chip **10**, 563 (2010).